Star formation rates from young-star counts and the structure of the ISM across the NGC 346/N66 complex in the SMC[★]

S. Hony,[1][†] D. A. Gouliermis,[1,2] F. Galliano,[3] M. Galametz,[4] D. Cormier,[1]
C.-H. R. Chen,[5] S. Dib,[6,7] A. Hughes,[2,8,9] R. S. Klessen,[1,10,11] J. Roman-Duval,[12]
L. Smith,[13] J.-P. Bernard,[8,9] C. Bot,[14] L. Carlson,[15] K. Gordon,[12,16] R. Indebetouw,[15,17]
V. Lebouteiller,[3] M.-Y. Lee,[3] S. C. Madden,[3] M. Meixner,[12,18] J. Oliveira,[19]
M. Rubio,[20] M. Sauvage[3] and R. Wu[21]

Affiliations are listed at the end of the paper

ABSTRACT

The rate at which interstellar gas is converted into stars, and its dependence on environment, is one of the pillars on which our understanding of the visible Universe is build. We present a comparison of the surface density of young stars ($\Sigma_\star$) and dust surface density (Σ_{dust}) across NGC 346 (N66) in 115 independent pixels of $6 \times 6 \, \mathrm{pc}^2$. We find a correlation between $\Sigma_\star$ and Σ_{dust} with a considerable scatter. A power-law fit to the data yields a steep relation with an exponent of 2.6 ± 0.2. We convert Σ_{dust} to gas surface density (Σ_{gas}) and $\Sigma_\star$ to star formation rate (SFR) surface densities (Σ_{SFR}), using simple assumptions for the gas-to-dust mass ratio and the duration of star formation. The derived total SFR ($4 \pm 1 \times 10^{-3} \, \mathrm{M_\odot \, yr^{-1}}$) is consistent with SFR estimated from the Hα emission integrated over the Hα nebula. On small scales the Σ_{SFR} derived using Hα systematically underestimates the count-based Σ_{SFR}, by up to a factor of 10. This is due to ionizing photons escaping the area, where the stars are counted. We find that individual $36 \, \mathrm{pc}^2$ pixels fall systematically above integrated disc galaxies in the Schmidt–Kennicutt diagram by on average a factor of $\sim$7. The NGC 346 average SFR over a larger area (90 pc radius) lies closer to the relation but remains high by a factor of $\sim$3. The fraction of the total mass (gas plus young stars) locked in young stars is systematically high ($\sim$10 per cent) within the central 15 pc and systematically lower outside (2 per cent), which we interpret as variations in star formation efficiency. The inner 15 pc is dominated by young stars belonging to a centrally condensed cluster, while the outer parts are dominated by a dispersed population. Therefore, the observed trend could reflect a change of star formation efficiency between clustered and non-clustered star formation.

Key words: stars: pre-main-sequence – ISM: individual objects: NGC 346 – ISM: structure – Magellanic Clouds.

1 INTRODUCTION

It is generally accepted that the local star formation rate (SFR) scales with the local gas density of the interstellar medium (ISM). This wisdom is captured in the Schmidt–Kennicutt relation (SK relation; see for a review Kennicutt & Evans 2012) which connects the observed gas-surface density (Σ_{gas}) along various sight-lines with the observed surface density of SFR (Σ_{SFR}). Even though there are multiple incarnations of the SK diagram, depending on

which tracers are used to measure both Σ_{gas} and Σ_{SFR}, and whether to consider only the dense (molecular) gas or include the atomic phase, the emerging picture is clear: the higher the ISM column density, the higher the SFR. A key feature of the SK relation is its power-law behaviour over a large dynamic range of gas column densities and SFRs. The slope of the relation depends on whether one measures only the dense gas (exponent $\sim$1) or also the atomic gas (exponent $\sim$1.4).

The physical interpretation of this interdependence, i.e. how to derive the efficiency with which interstellar gas is converted into stars, is much less self-evident, especially on small spatial scales ($<$1 kpc). This is due to the following. (i) The 'SFR' measures stars that have already formed, while the gas column density relates

to (the capacity for) future star formation (SF). On small scales, with low numbers of stars, one can no longer expect to measure a time-averaged efficiency as is the case when averaging over a large number of star-forming sites. (ii) Dynamical simulations (e.g. Kiseleva et al. 1998) and observations (e.g. Goodman 2004) show that young stars may be displaced, by several pc per Myr, from the location where they were born, and thus removed from the reservoir of gas from which they formed. (iii) The large-scale averages include non-star-forming parts of the ISM, and the relative proportion of this 'inactive' gas will change when zooming in on smaller scales. (iv) Many of the used SFR tracers [e.g. Hα or far-ultraviolet (FUV) emission] are sensitive only to high-mass stars, which represent only a fraction of the stellar mass assembled in the SF event, and to derive the total SFR one needs to extrapolate the mass function to lower masses. Since the high-mass slope of the initial mass function (IMF) is very steep – very few of the formed stars are high mass – the corrections are large and sensitive to the assumed shape of the IMF. Some or all of these effects are probably the reason why the studies of SFRs in nearby individual molecular clouds (Evans et al. 2009; Heiderman et al. 2010; Wu et al. 2010; Gutermuth et al. 2011) find very different SFRs at a given gas column density compared to global averages.

The aim of this paper is to circumvent some of these complications by studying the correlation between newly formed stars and the gas reservoir (Σ_{SFR} and Σ_{gas}) in many small beams ($\sim$6 pc) which cover an entire star-forming complex. We investigate, thus, the small-scale relation between young stars and gas reservoir while covering a larger region. We use the most direct way of determining Σ_{SFR}, i.e. by counting the newly assembled stars. At the same time we employ the 'dust method' to determine the ISM column density, i.e. using the infrared (IR) to submillimetre (submm) dust continuum emission to derive dust surface densities. This method has the advantage of not being sensitive to the state of the gas (ionized, neutral or molecular) as long as dust and gas are well mixed. This insensitivity is important because we will use a catalogue of low- and intermediate-mass pre-main-sequence (PMS) stars plus upper-main-sequence (UMS) stars, i.e. O- and B-type stars, as the basis for our star counts. Due to the evolutionary stage of the PMS stars – a few Myr after the onset of SF – the parental molecular complex may have been subject to significant photodissociation and using a molecular gas tracer (such as CO) may lead to an incomplete view of the total gas surface densities.

The object of choice is the star-forming complex related to NGC 346, also often referred to as N66. NGC 346 is the most prominent SF region in the Small Magellanic Cloud (SMC). In order to assess the Σ_{SFR}, an unbiased census of the young stellar population is required. This is available for NGC 346 thanks to *Hubble Space Telescope* (*HST*) observations (Gouliermis et al. 2006; Nota et al. 2006, see Section 3.1). We have access to sensitive IR-to-submm photometry from *Spitzer* (PI: Gordon), *Herschel* (PI: Meixner) and Atacama Pathfinder EXperiment (APEX)/LABOCA [Large APEX (Atacama Pathfinder Experiment) Bolometer Camera] (PI: Hony) in order to derive reliable dust surface densities. The proximity (60 kpc) of the SMC in combination with the size of the star-forming complex ($\sim$100 × 100 pc^2) enables us to 'zoom in' ($\sim$6 pc linear scale) and study local variations at the angular resolution of the available submm observations.

Moreover, the entire complex encompasses a range of environments. In terms of the ISM, the region exhibits a wide range of surface brightness of hot dust (24 μm), polycyclic aromatic hydrocarbon (PAH; 8 μm) and molecular gas (CO($J = 2$–1); Rubio et al. 2000). In terms of the stellar content, there are zones which

are cluster dominated as well as regions where the young stars are more dispersed (Gouliermis, Hony & Klessen 2014). This allows us to examine how the environment influences the relation between SF and the available ISM reservoir. The main questions we address are as follows.

(i) How well do young stars and the densest ISM track each other?

(ii) Do star counts yield the same Σ_{SFR} as indirect tracers?

(iii) Does the efficiency of SF vary between clustered and more extended spatial distributions?

(iv) What is the effect of averaging over different scales on the derived parameters in the position in the SK diagram?

Additionally, we examine whether there may be an effect of the reduced metal abundance of the SMC (0.2 solar; Haser et al. 1998) on the star formation efficiency (SFE).

The paper is organized as follows. Previous work on deriving SFR from individual young sources is reviewed in Section 2. In Section 3 we present the catalogue of young stars and the IR-to-submm data sets that we use for our analysis. We further describe the data treatment to derive independent surface density measurements in 20 × 20 arcsec^2 (6 × 6 pc^2) beams (Section 3.4). Our methodology to obtain gas surface densities, using spectral energy distribution (SED) fitting, is described in Sections 4.1 and 4.2. The SFR derived from our young-star counts is compared to indirect SFR tracers in Section 4.3. In Section 5 we compare the derived Σ_{gas} and Σ_{SFR}. Possible biases that may affect the observed value of Σ_{SFR} /Σ_{gas} are discussed in Section 6. We conclude in Section 7.

2 PREVIOUS WORK

Most of the work done on comparing ISM column densities and SFRs based on individual objects has concentrated on nearby (within 1 kpc from the Sun) Milky Way star-forming sites (Evans et al. 2009; Heiderman et al. 2010; Lada, Lombardi & Alves 2010; Wu et al. 2010; Gutermuth et al. 2011). These studies have consistently shown that when one considers the immediate dense environment (on a few parsec scales) surrounding the newly formed stars, the derived SFR is higher than predicted by the galaxy-averaged SK relation (by up to a factor of 54) for a given ISM column density.

Evans et al. (2009) and Lada et al. (2010) present the total SFRs based on young stellar object (YSO) candidates, identified from their mid-IR excess using *Spitzer* and compare those to molecular cloud masses derived using extinction maps for $\sim$10 nearby molecular clouds. These studies show that there is a large variety of SFE among those clouds. Lada et al. (2010) show that some of the observed spread in SFE disappears when considering only the mass of gas above an extinction threshold of $A_K > 0.8$ mag. They interpret this as an indication for a density threshold below which SF does not occur. A similar conclusion is reached by Heiderman et al. (2010) who study the Σ_{SFR} versus Σ_{gas} within those clouds using YSOs. The typical spatial scale over which they compare these quantities is from a few tenths of a parsec to a few parsec. Their data show a very sharp decrease in Σ_{SFR} below $\Sigma_{gas} \approx 10^2$ M$_\odot$ pc^{-2} which is interpreted as resulting from a density threshold for SF. Note that such a threshold, if it exists, cannot be a *universal* threshold. There are several observations of specific regions whose gas surface densities exceed the threshold, with much less SF than would be expected (e.g. Longmore et al. 2013; Rathborne et al. 2014). Moreover, the existence of a column density threshold for SF in a turbulent ISM is not supported by theoretical models (Clark & Glover 2014).

A different picture emerges from the analysis presented by Guter-muth et al. (2011). These authors present scatter diagrams of surface density of YSOs versus Σ_{gas} (from extinction) for eight molecular clouds within 1 kpc from the Sun. They find a steep power-law correlation (with indices between 1.4 and 2.7, with an outlier at 3.8) with significant scatter and no indication for a density threshold. They argue that the data are consistent with an SFR which is pro-portional to Σ_{gas}^2. Note that the different conclusion reached by the latter authors is based, in part, on the way the surface density of YSOs is calculated in the low-surface-density regime as they use the *n*th nearest neighbour centred on the detected YSOs. We further note that, given the steep dependence on Σ_{SFR} and the low number counts, distinguishing between a threshold and this power law is difficult and almost a matter of semantics.

The work by Gutermuth et al. (2011) is the Galactic study that can be compared most directly to the NGC 346 analysis we present here, because their Σ_{gas} maps cover several tens of parsecs around the molecular clouds and each cloud harbours a significant number (>100) of YSOs. Compared to the work we present here, these previous studies have the advantage of proximity and as a result, they are able to examine the SF within individual molecular clouds on spatial scales of <1 pc while the best angular resolution we can attain in the SMC in the ISM tracers is ∼6 pc.

Recent *Spitzer* surveys of the Large and Small Magellanic Clouds (LMC and SMC) made it possible to use resolved massive YSOs to determine current SFRs outside of the Galaxy. Unlike the con-sistently higher SFRs of small-size clouds reported in the afore-mentioned Galactic studies, Chen et al. (2010) showed that current SFRs determined from massive YSOs in individual giant molec-ular clouds in H II complexes in the LMC are distributed above and below the SK relation, depending on the evolutionary states of the giant molecular cloud. The scatter in SFR diminishes and follows the SK relation when properties are averaged over the en-tire H II complexes of 150–200 pc. This is in agreement with the findings of Kruijssen & Longmore (2014), who attribute the scatter on smaller scales to incomplete statistical sampling of independent star-forming regions. Furthermore, the commonly used SFR trac-ers such as Hα and 24 μm luminosities would underestimate the amount of SF in regions not actively producing O-type stars, such as the LMC's largest molecular ridge and the Magellanic Bridge. They show that using Hα or 24 μm as SFR tracers these points are outliers on the SK relation while they follow the SK relation when using SFR determined from YSO counts (Indebetouw et al. 2008; Chen et al. 2014).

The work presented here differs from these previous studies by the sources we use to trace the SF (PMS+UMS stars versus YSOs) and the way we derive the ISM column densities (dust emission versus extinction). This has the following (dis-)advantages.

(i) Rich stellar catalogue: *HST* has provided accurate photometry for more than 5000 stellar sources covering the PMS (Gouliermis et al. 2006).

(ii) Measured mass function and age: ages and the mass functions have been determined for the UMS+PMS stellar catalogue (Sabbi et al. 2008). This means we can rely on the observed mass function, which covers a significant (0.8–40 $M_{\odot}$) part of the entire mass range, and the observed duration of the SF event to derive the SFR. The YSO studies assume a typical age and mass for a YSO, both of which are uncertain (e.g. Preibisch 2012), which could introduce a large *systematic* uncertainty.

(iii) Large coverage: the IR and submm observations that we use to measure dust column densities are very sensitive and most cover

the entire SMC (Section 3.2). As a result, we have access to an unbiased probe of the dust surface density out to large distances and low column densities. This is important to assess the behaviour of the SFR at low Σ_{gas}, where significant disagreement exists in the literature (see above).

However, since we are using stars that are no longer embedded, the sources in our catalogue are more evolved (<5 Myr, Section 3.1) than YSOs (<2 Myr) and have had more time to displace (or be displaced from) their parental gas reservoir. Moreover, since the whole region has to be more evolved for it to host so many PMS stars, the radiation from the hot, young stars has had more time to affect the surrounding medium.

3 OBSERVATIONS

3.1 Young stellar catalogue

Imaging with the *HST* of star-forming regions in the Magellanic Clouds has provided access to exceptionally rich samples of newly born stars down to the sub-solar regime over large areas of the sky. Our catalogue of young stars in NGC 346, one of the largest star-forming complexes in the SMC, is among the richest Mag-ellanic Clouds stellar ensembles ever collected with *HST*. Three pointings (with significant offsets), centred on NGC 346, were ob-served with the Wide-Field Channel of ACS covering an area of about 5×5 arcmin^2 (∼88×88 pc^2). The images were obtained within the *HST* programme GO-10248 (PI: Nota; Nota et al. 2006) in the filters *F555W* and *F814W* (equivalent to the standard *V* and *I* bands). Detailed descriptions of the data reduction and photometry are given in Gouliermis et al. (2006). The photometry reveals more than 98 000 stars at various evolutionary stages, and its 50 per cent completeness limit is $m_{555} \simeq 27$ (Gouliermis et al. 2006).

The sample of young stellar populations in NGC 346 consists of the low-mass PMS stars, which are identified from their faint-red positions on the colour–magnitude diagram (CMD). See Goulier-mis (2012) for a review on low-mass PMS stars in the Magellanic Clouds. This sample is complemented by the UMS stars (selected with colours $m_{555} - m_{814} \leq 0.0$ and magnitudes $12 \sim m_{555} \lesssim 17$), including more than 30 early-type stars (see also Massey, Parker & Garmany 1989; Mokiem et al. 2006). The masses of the selected UMS stars are such that they would have evolved off the main sequence if they were older than the PMS population. Thus, the catalogue we use in this analysis contains 5150 young (PMS and UMS) stars in the mass range between ∼0.5 and ∼40 $M_{\odot}$. The location of the young stars within the complex is indicated in Fig. 1 with yellow contours. This image shows the very prominent Hα emission associated with the central cluster and the presence of several secondary clusters of young stars to the north which cause little Hα emission.

It is hard to get accurate age and mass determinations of the *indi-vidual* PMS stars based on their position in the CMD (Jeffries 2012). An isochronal median age around ∼3 Myr has been defined for the *ensemble* of PMS stars in NGC 346 on the basis of comparison with evolutionary models (Sabbi et al. 2008; Cignoni et al. 2011). Mokiem et al. (2006) have spectroscopically studied the high-mass stars towards NGC 346. They find ages between 0 and 5 Myr for the high-mass stars that belong to the SF complex. This age range is fully compatible with the position and spread of the low-mass PMS stars in the CMD. Since our objective is to measure the *average* SFR counting *all* stars that have formed during the SF event, we use 5 Myr as the star formation duration (Δt_{SFR}). Thus, Δt_{SFR} refers
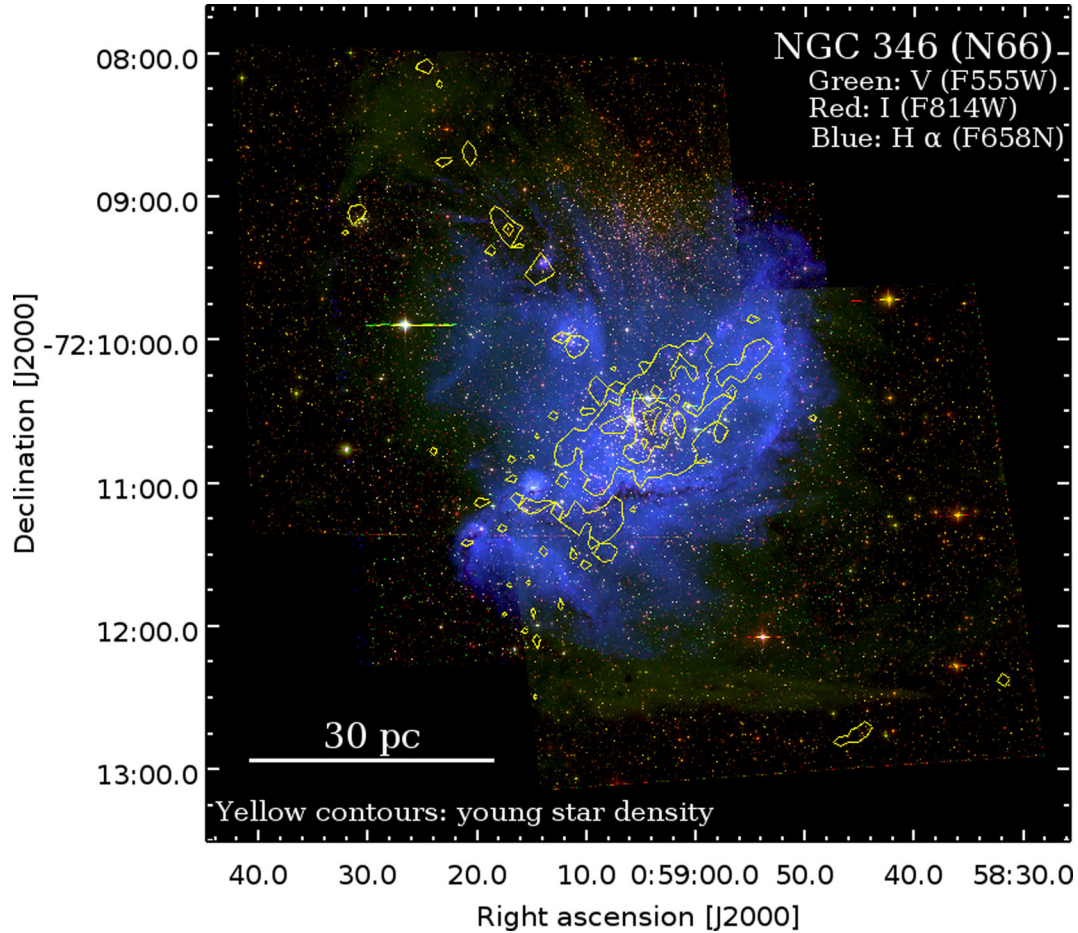
Figure 1. False colour composite image (green: optical, red: IR, blue: Hα) of NGC 346 based on *HST* imaging (PI: Nota; Nota et al. 2006). The contours of the, 2 arcsec resolution, density map ($\Sigma_\star$) of the young stars are shown in yellow. The contour levels correspond to 3, 10 and 20 stars pc^{-2}. The maximum value of $\Sigma_\star$ is 45 stars pc^{-2}.

to the duration of the event *not* to the ages of the individual stars. Therefore, this approach is conceptually different from the YSO-counting studies (e.g. Heiderman et al. 2010; Lada et al. 2010) in which ages of the individual objects have been assumed.

We construct the entire mass function of the UMS+PMS catalogue by extrapolating the mass function for masses above 0.8 M$_\odot$ derived by Sabbi et al. (2008, fig. 3 bottom panel) from the same observational material. Their mass function is completeness corrected for crowding and photometric sensitivity but not for interstellar extinction. Over the measured range the mass function has a slope of -1.43.[1] We extrapolate to lower masses using a Kroupa mass function with a slope of -0.3 between 0.08 and 0.5 M$_\odot$ and a slope of 0.7 between 0.01 and 0.08 M$_\odot$ (Kroupa 2001). The total stellar mass formed in the last 5 Myr, obtained by integrating this mass function and multiplying by the survey area (88 × 88 pc^2), equals $\sim 2.24 \times 10^4$ M$_\odot$. Since we have 5150 stars in our catalogue, each source represents on average a mass of 4.3 M$_\odot$ (M_{cat}). The mass in directly detected stars ($M_\star > 0.8$ M$_\odot$) is 1.2×10^4 M$_\odot$, i.e.

50 per cent of the total. The main parameters used in our analysis are summarized in Table 1.

The total SFR, averaged over the last 5 Myr, of the complex calculated in this way is $4 \pm 1 \times 10^{-3}$ M$_\odot$ yr^{-1}, where the uncertainty takes into account possible SF outside of the field of view of *HST* (20 per cent) and the extrapolation of the observed mass function to lower masses (20 per cent) but not the systematic uncertainty due to the assumed duration of the SF event. This value is consistent with the results of Simon et al. (2007) who find an SFR > 3.2×10^{-3} M$_\odot$ yr^{-1} over the last 1 Myr using *Spitzer* identified YSO candidates.

For the rest of the analysis, we assume that the mass function and the duration of SF are invariant across the star-forming complex. There are some indications of variations in the slope of the mass function in NGC 346 (Sabbi et al. 2008; Cignoni et al. 2011). The general trend is a steepening of the slope with increasing distance to the central cluster, i.e. a larger fraction of high-mass stars towards the central cluster, consistent with a certain degree of mass segregation in the cluster. However, such variations have little impact on our results which are based on star counts, while luminosity-based SFR tracers (e.g. Hα) are very sensitive to the number of high-mass stars and thus the high-mass slope of the mass function. As an illustration of this invariance consider the standard Kroupa mass function (Kroupa 2001) with a high-mass power-law slope of -1.3. When we vary this slope between -1.0 and -2.0 – the observed range of

[1] We use the formalism of the mass function $-\log_{10}(N(\Delta\log_{10}(m)))$ versus $\log_{10}(m)$ – as given by Scalo (1986). In this definition, the Salpeter mass function has a slope of -1.35 and the Kroupa mass function has a slope of -1.3 above 0.5 M$_\odot$.

Table 1. Values and symbols used throughout this paper.

Quantity	Symbol	Value	Comments/refs
SMC distance	d_{SMC}	60 ± 3 kpc	Harries, Hilditch & Howarth (2003)
Detected young stars	N_{star}	5150	Gouliermis et al. (2006), see Section 3.1
Total young stellar mass	M_{tot}	2.2×10^4 M$_\odot$	Sabbi et al. (2008), see Section 3.1
Mass per catalogue source	M_{cat} [a]	4.3 M$_\odot$	$= M_{tot} N_{star}^{-1}$, see Section 3.1
SF duration	Δt_{SFR}	5×10^6 yr	Mokiem et al. (2006), see Section 3.1
Gas-to-dust mass ratio	r_{gd}	1250	Section 4.2
Derived quantity			
Young-star surface density	$\Sigma_\star$		From star catalogue
Stellar mass surface density	$\Sigma_{M_\star}$		$= \Sigma_\star \times M_{cat}$
SFR surface density	Σ_{SFR}		$= \Sigma_{M_\star} \Delta t_{SFR}^{-1}$
Dust surface density	Σ_{dust}		From SED fitting
Gas surface density	Σ_{gas}		$= \Sigma_{dust} \times r_{gd}$
Stellar mass fraction	$frac_{M_\star}$		$= \Sigma_{M_\star} (\Sigma_{M_\star} + \Sigma_{gas})^{-1}$

Notes. [a]This mass is *not* the mean mass of the *HST* detected sources but the mass each source represents after correcting for completeness. The mean mass of the young stars in the *HST* catalogue is ~ 2 M$_\odot$.

slopes in NGC 346 (Sabbi et al. 2008) – the total mass per number of stars above 0.8 M$_\odot$ (i.e. M_{cat}) varies by only ~ 20 per cent. For the same variations in slope, the fraction of mass locked in the high-mass stars – those powering the Hα emission ($M_\star > 8$ M$_\odot$) – varies by 1500 per cent!

3.2 *Herschel* and *Spitzer* data

We use the mid-IR-to-submm photometric maps that have been obtained with *Spitzer* (SAGE-SMC; Gordon et al. 2011) and *Herschel* (HERITAGE; Meixner et al. 2013). Within these two large programmes the entire SMC has been observed at IRAC (3.6, 4.5, 5.8 and 8.0 μm), MIPS (24, 70 and 160 μm), PACS (100 and 160 μm) and SPIRE (250, 350 and 500 μm) wavelengths. The sensitivity of these data sets is such that for the environment of the prominent star-forming region NGC 346, the photometric uncertainty is dominated by the absolute flux calibration (see also Section 3.4). An overview of NGC 346 in some key ISM tracers is shown in Fig. 2. In the following analysis, we mainly use the IRAC, MIPS 24, MIPS 70, PACS 100, PACS 160 and SPIRE 250 data, because these sufficiently cover the SED to derive accurate dust surface densities at optimal angular resolution (~ 20 arcsec). The SPIRE 350 and 500 μm data have poorer angular resolution. The only exception is the dust masses derived within large circular apertures (Table 2) which uses the SPIRE 350 μm data to replace the LABOCA because the latter is not observed over such a large area.

3.3 LABOCA 870 μm imaging data

To constrain the emission by the coolest dust, we use LABOCA data at 870 μm, instead of the SPIRE 350 data. This data set allows us to obtain measurements at ~ 20 arcsec resolution which is unattainable with *Herschel*/SPIRE 350 and 500. LABOCA is a multichannel bolometer array for continuum observations at 870 μm installed on the APEX telescope in Chile. It has a field of view of 11.4 arcmin and a point spread function full-width at half-maximum of 19.2 ± 0.3 arcsec. Observations of the NGC 346 region with LABOCA were carried out in 2008 December and 2009 April, May and September (programme ID: O-081.F-9329A-2008; PI: Hony). The mapping was done with a raster of spiral pattern in order to fully sample the final map (size of the region mapped: 25×25 arcmin^2). Data are reduced with the Bolometer Array

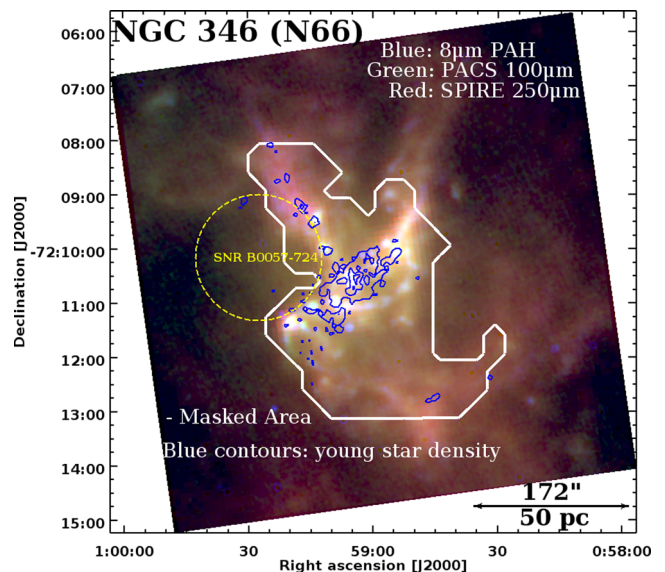**Figure 2.** False colour image showing an overview of the large environment of NGC 346 in key ISM tracers. We show 8 μm emission indicative of the location of the most prominent Photon-Dominated Regions (PDRs) (blue; IRAC4 emission minus the stellar continuum estimated from IRAC2), the warmer dust traced by PACS 100 (green) and the cooler dust (SPIRE 250, red). Each waveband is shown at its native resolution. The blue contours show the stellar density (see Fig. 1). The general observed trend is a decreasing dust temperature with distance to the most rich cluster (yellow to red colour gradient) and strong PDRs near (but not peaking on) the stellar concentrations. The region where both dust surface density, including LABOCA measurements, and stellar densities are well defined is indicated by the white line (see Section 3.4 for details).

Analysis software (Schuller et al. 2010). The scans are reduced individually. They are calibrated using the observations of planets (Mars, Neptune, Uranus, Venus) and secondary calibrators (G10.62, G5.89, HLTAU, PKS0506.61, PMNJ0210-5101, PMNJ0303-6211, PMNJ0450-8100, N2071IR and VY-CMa). We determine zenith opacities using a linear combination of the opacity determined using sky-dips and that computed from the precipitable water vapour.[2]

[2] Tabulated sky opacities are provided at http://www.apex-telescope.org/bolometer/laboca/calibration

Table 2. Total dust mass, gas consumption time-scale and integrated SFE as a function of the area considered in the analysis. The first row corresponds to the area included in the pixel-by-pixel analysis. A radius of 52 pc is equivalent to the area covered by the *HST* observations. The 90 pc radius matches the prominent SPIRE 250 and 350 μm waveband emission, while the largest radius probes the full extent of the Hα nebula around NGC 346. The gas consumption time-scale (τ_{gas}) is defined as the M_{gas}/SFR and the integrated star formation efficiency ($SFE_{10\,Myr}$) is calculated as the percentage of gas that will be converted into stars after 10 Myr, assuming that the SFR remains constant. We use 10 Myr as the limiting age, when supernovae might disrupt the ISM and halt the SF.

Area/radius	M_{dust} ($M_\odot$)	τ_{gas} (10^8 yr)	$SFE_{10\,Myr}$ (per cent)
Mask	498 ± 18 per cent	1.7	5.8
52 pc	900 ± 19 per cent	2.5	4.0
90 pc	1616 ± 19 per cent	4.5	2.2
145 pc	2741 ± 22 per cent	7.6	1.3

We remove dead or noisy channels as well as stationary points or data taken at fast scanning velocity or above an acceleration threshold. We subtract the correlated noise, apply steps of median noise removal, baseline correction and despiking. The reduced scans are then combined into a final map. We isolate the pixels above a given signal-to-noise ratio to define a 'source model' that is subtracted from the time-ordered data. We rerun the reduction pipeline and add the source model to the time-ordered data to obtain a new map. The process is iterated until the result map converges (five iterations were applied for NGC 346).[3] The final map is shown in Fig. 3. Within the region of interest, there are three main emission features. There is an emission peak towards the central cluster, a direct indication that this sight-line is dust rich. We detect a brighter emission peak towards the north-west of the main cluster and a plume of 870 μm emission which follows the string of stellar clustering towards the north-west. This plume coincides with the brightest CO(*J* = 2–1) emission detected in the region (Rubio et al. 2000). Due to the median filtering that is applied to remove the atmospheric and telescope signal, any spatially very extended emission has been removed as well. This explains why we do not detect any free–free emission from the ionized gas which should be present in this region (see Fig. 3).

3.4 Beam-matched data

In our analysis, we use maps with a resolution of 20 arcsec (6 pc at the distance of the SMC). All maps with intrinsic spatial resolutions better than this resolution, including the stellar catalogue, have been convolved to the this effective spatial resolution. LABOCA, MIPS 70 and SPIRE 250 maps have not been convolved since they already have an intrinsic spatial resolution very close to 20 arcsec. We use the convolution kernels available from Karl Gordons web page[4] for convolving to the SPIRE 250 beams. For the stellar density map – which has an exceedingly good intrinsic angular resolution – we have directly convolved the 2 arcsec stellar density map with the SPIRE 250 μm beam. After convolution, all maps have been re-projected on the same pixel scheme with pixel size
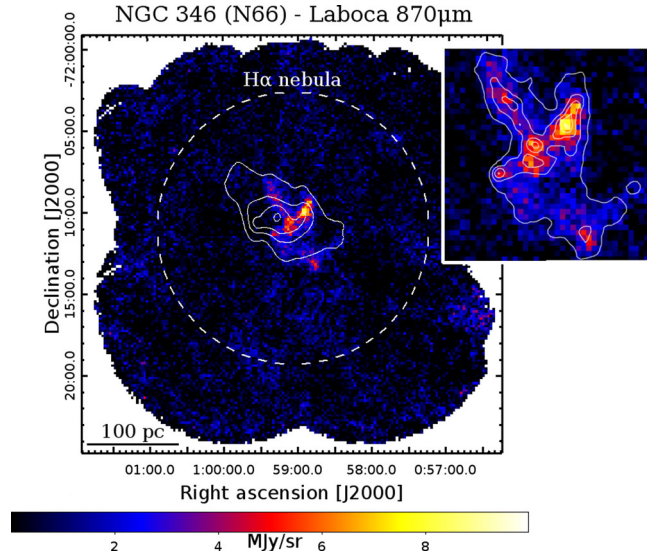

Figure 3. LABOCA 870 μm map of NGC 346. The contours show the 36 cm radio continuum emission from SUMSS (Mauch et al. 2003). The 3 and 6 cm radio continuum images (not shown) exhibit the same morphology (Dickel et al. 2010). The possible corresponding contribution of free–free emission at 870 μm has been filtered out by the median filtering applied in the data reduction process. The dashed circle indicates the approximate extent of the Hα nebula. We show a close-up of the brightest region in the inset, in which the 250 μm dust emission contours, in perfect correspondence with the LABOCA map, are shown.

of 20×20 arcsec[2] in order to have spatially independent measurements and to allow pixel-by-pixel SED extraction and comparison between the stellar densities and derived dust surface densities. We use the program SWARP from AstroMatic[5] for calculating the re-projected maps, as it is according to our experience the most accurate tool in conserving the mean surface brightness. This is particularly true when re-projecting to a pixel scheme with very different pixel sizes, which is our case.[6]

In order to create reliable random noise maps that represent well the noise in the original maps and the effects of convolution and re-projection, we apply the following procedure.

(i) The amplitude of the noise in each map has been estimated by measuring the median absolute deviation (MAD) from the median. This value is a more robust measure of the noise in a map than the standard deviation in the presence of real source emission. The estimated standard deviation equals $1.4825 \times$ MAD.

(ii) We generate a pure noise map at the original resolution using the measured standard deviation.

(iii) We generate a projected noise map convolving and re-projecting this noise map in the exact same manner as we do for the science map.

(iv) We measure the amplitude of the noise in the projected noise map as the standard deviation of the fitted Gaussian function to the histogram of pixel values.

These output noise levels have been compared to the formal calibration uncertainties (expressed as percentages of the observed surface brightness levels). For all maps except the LABOCA map,

---

[3] More details on the techniques are provided in Galametz et al. (2013).
[4] http://dirty.as.arizona.edu/~kgordon/mips/conv_psfs/conv_psfs.html

[5] http://www.astromatic.net
[6] The IDL/astrolib tool *hastrom*, often used for the same purpose, performs poorly in this case.

the absolute calibration is dominant throughout the region of interest. In the case of the LABOCA map, we retain for each pixel in the projected noise map the larger value of the flux calibration uncertainty and the random noise value. These uncertainties should not be added (quadratically) because the LABOCA flux calibration uncertainty reflects the scatter in the measured calibrator fluxes and is thus, in essence, also a random noise term.

Pixels outside the area surveyed by *HST* and pixels where the LABOCA measurement is less than 2σ are masked. There are 115 valid, independent 20×20 arcsec^2 pixels (covering about $\sim$4000 pc^2) in the following pixel-by-pixel analysis. Their outline is shown in Fig. 2. All maps at the other wavelengths have signal-to-noise ratios larger than 2 – in most cases much larger – in these pixels.

4 DUST, GAS AND SFR SURFACE DENSITIES

4.1 SED fitting

In order to derive dust surface densities, we fit the IR-to-submm dust continuum SED for each independent pixel in the region. The dust emission fitting is performed with the Galliano et al. (2011) SED model. This model accounts for variations of dust excitation rates along the line of sight. Following the prescription of Dale et al. (2001), it assumes that the distribution of dust mass, $M_{\rm dust}$, is parametrized by the starlight intensity, U, as a power law: $dM_{\rm dust}/dU \propto U^{-\alpha}$, between $U_{\rm min}$ and $U_{\rm min} + \Delta U$. The parameter U is the stellar flux received by the dust and is normalized to the solar neighbourhood value (Mathis, Mezger & Panagia 1983). The shape of the SED (in particular, both its peak wavelength and its width) constrains the parameters of this power law.

For a given starlight intensity, U, the dust emissivity is derived from the Zubko, Dwek & Arendt (2004, dust family: BARE-GR-S) model, designed to fit the diffuse Galactic emission. However, we replace graphite by amorphous carbon (Zubko et al. 1996, ACAR). Indeed, Galliano et al. (2011) showed that the standard Galactic grain properties applied to *Spitzer* and *Herschel* observations of the LMC lead to violation of elemental abundance constraints, while the modified composition (the 'AC model') gives realistic gas-to-dust mass ratios. In summary, we make the assumption that grains in the SMC will have similar optical properties as in the LMC.

The choice of a set of grain emissivities is tainted by systematic uncertainties. As demonstrated by Galliano et al. (2011), the derived dust mass changes by a factor of 2–3 depending on the optical properties. However, it is also shown that the change is essentially a simple scaling of the dust mass, and does not significantly affect the trends. Besides, if the origin of the difference in emissivity between the Milky Way and the LMC is an evolutionary effect, linked to metallicity (cf. Planck Collaboration XVII 2011), it is likely that using LMC emissivities puts us closer to the reality than simply assuming Galactic properties.

The fit of the observed SED, with the previously described dust model, provides constraints on the dust mass, $M_{\rm dust}$; the parameters of the power-law distribution of starlight intensities, $U_{\rm min}$, ΔU and α, which we summarize by quoting the average starlight intensity, $\langle U \rangle$; and the PAH mass fraction, normalized to the Galactic value, $f_{\rm PAH}$. In order to estimate the final uncertainties on these derived dust parameters, we perform Monte Carlo iterations, following the method described in Galliano et al. (2011), taking into account the correlation between calibration uncertainties. The median uncertainties on the derived parameters (σ_x/x) are 6 per cent for $L_{\rm dust}$, and
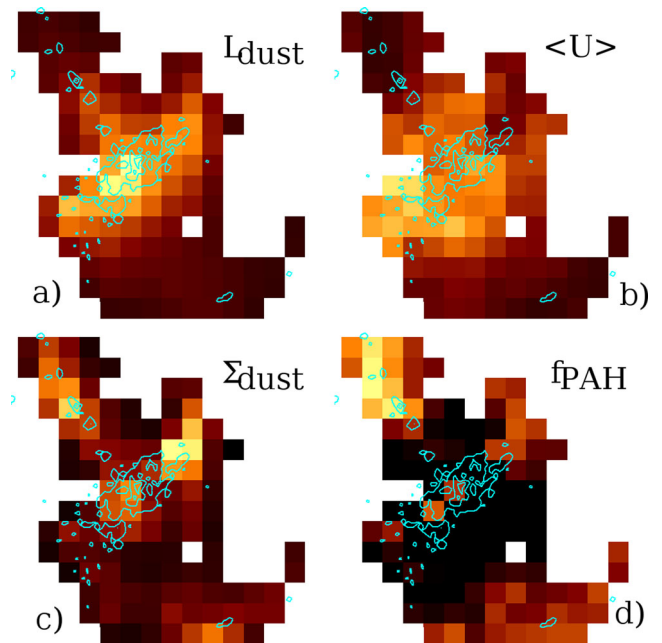

Figure 4. Maps of the output parameters of the dust SED fitting. The region shown corresponds to the white contour in Fig. 2. For reference, we show the surface density map of young stars in contours (see Fig. 1). We show the luminosity of the dust emission ranging from 150 to 1300 L$_\odot$ (a), the average radiation field as experienced by the dust ranging between 6 and 45 G$_0$ (b), dust surface density ranging from 0.05 to 0.3 M$_\odot$ pc^{-2} (c) and the mass of PAHs relative to the total dust mass normalized to the Galactic value ranging from 0 to 0.3 (d).

19 per cent for $\Sigma_{\rm dust}$ and $\langle U \rangle$. The median standard deviation on $f_{\rm PAH}$ is 0.02.

Maps of the best-fitting output parameters are shown in Fig. 4. One of the key results from the SED fitting which is evident from these maps is the clear distinction between the parameters which trace the heating of the dust (panels a and b) and the surface density of dust (panel c). Clearly the dust luminosity in the very active star-forming region NGC 346 (panel a) traces closely the radiation field. This is in stark contrast to other (more usual) observations of more diffuse regions where the incident radiation field (and dust temperature) does not vary much and $L_{\rm dust}$ traces the dust surface density. Panel d shows that the PAH abundance close to the main cluster is so low that their emission is undetectable in the broad-band photometry. This low abundance of PAH is in perfect agreement with the findings of Sauvage, Vigroux & Thuan (1990) who deduced an increased differential depletion of PAHs towards NGC 346 based on *IRAS* photometry. Similar paucities of PAHs towards other high-mass star-forming region in the Magellanic Clouds have been reported (e.g. Hony et al. 2010; Sandstrom et al. 2010).

4.2 Conversion of dust surface density to gas surface density

We assume that gas and dust are well mixed along each line of sight in which case the gas surface density ($\Sigma_{\rm gas}$) is proportional to the dust surface density ($\Sigma_{\rm dust}$) and the proportionality factor is the gas-to-dust mass ratio ($r_{\rm gd}$). The dust masses derived by SED fitting methods vary significantly and systematically (e.g. Galliano et al. 2011; Gordon et al. 2014) depending on the applied method and assumed dust optical properties. It is therefore important to use a value of $r_{\rm gd}$ consistent with the used SED fitting methodology, i.e. the value of $r_{\rm gd}$ that gives the correct gas mass given the derived dust

mass. We have calibrated the r_{gd} using the available gas tracers on a large scale. Within a 500 arcsec radius centred on NGC 346, we find an atomic gas mass of 2.7×10^6 M$_\odot$ using the Parkes+ATCA H I map (Kim et al. 2003) and a spin temperature of 60 K (Bernard et al. 2008). The molecular gas mass determined from CO($J = 1$–0) within the same aperture is 7.4×10^4 M$_\odot$ when using a CO-to-H$_2$ column density conversion factor (X_{CO}) of 10^{21} [cm^{-2} (K km s^{-1})$^{-1}$] (Bolatto, Wolfire & Leroy 2013). If we use an X_{CO} of 10^{22} [cm^{-2} (K km s^{-1})$^{-1}$], we find a molecular gas mass of 7.5×10^5 M$_\odot$. Such an elevated X_{CO} may be more appropriate given the harsh radiation field that is prevalent in the region, which may induce enhanced photodissociation of the CO molecules. Thus, we derive a total gas mass in the range of 2.7×10^6–3.4×10^6 M$_\odot$. The dust mass derived using the dust continuum photometry in this aperture and applying the same SED fitting routine we use for the pixel-by-pixel analysis yields 2.7×10^3 M$_\odot$. The derived r_{gd} ranges from ~ 1000 to ~ 1250. In the following, we use a fiducial value for r_{gd} of 1250, which is much higher than the Galactic value (100; Draine & Li 2007) due to the lower metallicity of the SMC. Our value for r_{gd} of 1250 is lower than the total SMC integrated value of 1740 from Gordon et al. (2014). The global value includes a significant amount of atomic gas at low column density in the outskirts of the SMC which is not detected in dust emission. This drives up the global r_{gd}.

Given that the derivation of r_{gd} is susceptible to significant *systematic* uncertainties in X_{CO} for the gas surface densities and dust optical properties for the dust surface densities, we will discuss the implications of a factor of 2 variations in the absolute value of r_{gd} on our results. Note that part of the purpose of this paper is to determine how well the ISM and stars follow each other on small spatial scales. This part of the analysis does not depend on the chosen absolute value for r_{gd}. The comparison of SFR and SFE with values derived for other regions is however sensitive to the chosen value and we will discuss the influence of our choice on the results we find.

We further assume r_{gd} to be invariant for the entire region. In principle, it is possible that r_{gd} could vary significantly, in particular in the vicinity of high-mass SF sites, where dust destruction can become important due to supernova explosions. Reid et al. (2006) have studied the supernova remnants within the large environment of NGC 346. These authors show that the region we study here appears largely unaffected by the impact of supernovae. The closest remnant they identified (SNR B0057−724, see also Fig. 2) lies to the north-east of the main cluster, outside of the region of interest. The observational data argue against strong variations of r_{gd} because they show that the ratio of dust heating to gas heating is very constant throughout the whole region (see Section 6.2).

4.3 SFR surface densities

The SFR map has been derived using the observed number of young stars along the line of sight in each pixel of the beam-matched stellar density map. It is calculated as (see also Table 1)

$$\mathrm{SFR} = \frac{N_\star M_{cat}}{\Delta t_{SFR}} = \frac{N_\star \times 4.3}{5 \times 10^6} [\mathrm{M}_\odot \, \mathrm{yr}^{-1}]. \qquad (1)$$

The star formation surface density map (Σ_{SFR}) is obtained by dividing this map by the area of a pixel in kpc^2.

In Fig. 5, we compare the derived Σ_{SFR} with selected, indirect SFR tracers. Note that we only compare with those tracers [$\Sigma_{H\alpha}$ – calibration from Hao et al. (2011) for a Kroupa IMF; $\Sigma_{24\,\mu m}$ – calibration from Rieke et al. (2009) and Σ_{TIR} – calibration from Murphy et al. 2011) which are appropriate for the very recent epoch
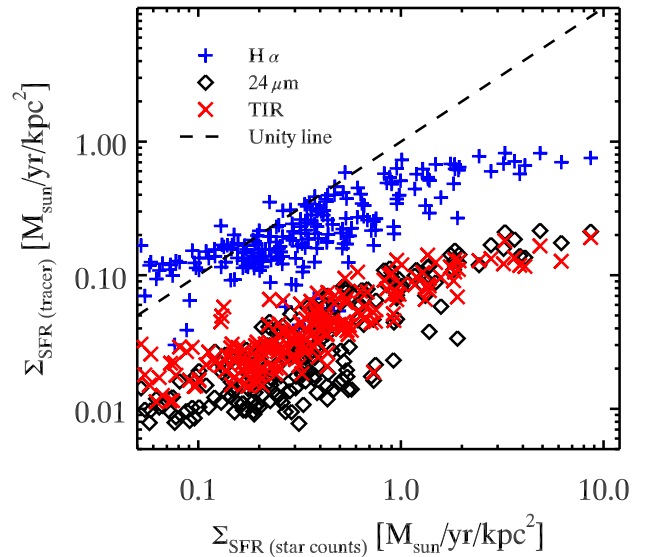

Figure 5. Comparison of derived pixel-by-pixel Σ_{SFR} using different methods. The *x*-axis shows the Σ_{SFR} using the young-star surface density. In blue we show Σ_{SFR} calculated following Hao et al. (2011, for the Kroupa IMF) using the continuum-subtracted Hα map from MCELS (Smith, Leiton & Pizarro 2000) that was kindly provided by S. Points. The red crosses are Σ_{SFR} estimates using the total infrared (TIR; 3–1100 μm) surface brightness following Hao et al. (2011) and the black symbols show the estimated Σ_{SFR} based on *Spitzer*/MIPS 24 μm (Rieke et al. 2009).
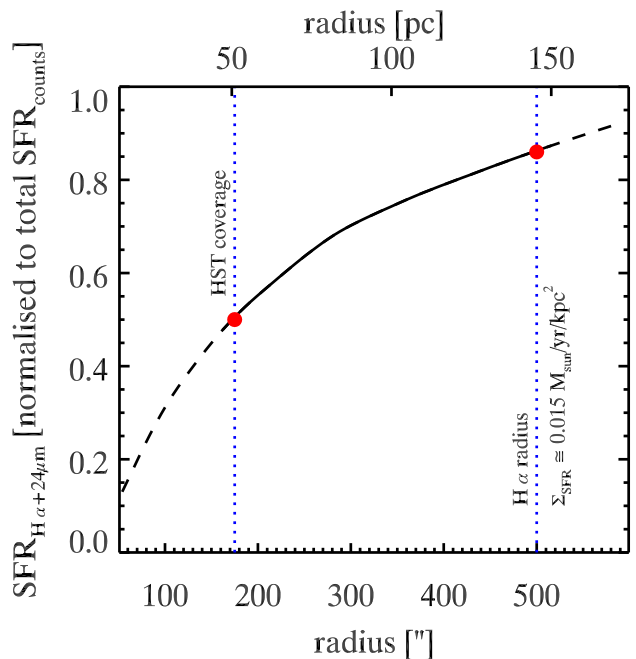

Figure 6. Derived total SFR for the NGC 346 complex based on the combined emission of Hα and 24 μm as a function of the radius (centred on $14°.776, -72°.1735$) over which the flux is integrated. We follow the prescription from Calzetti et al. (2007, equation 5). The SFR is expressed in terms of the fraction of the total SFR derived from star counts. The Hα and 24 μm emission are much more extended than the distribution of the young stars. As can be seen, the SFR derived within the radius of the *HST* coverage (~ 50 pc) is about half of the total SFR. Only when we integrate over the complete nebula (~ 500 arcsec), where the Hα emission reaches the diffuse background level do we derive similar SFR values.

of SF (<5 Myr) and we do not consider FUV because its calibration assumes a constant SFR over >10–100 Myr. As can be seen, the Σ_{SFR} from star counts is generally higher than those obtained from Hα or dust emission. Moreover, the differences are largest where the stellar density (i.e. Σ_{SFR}) is highest. Towards the densest cluster, the difference between counting stars and using Hα is a factor of 10, while the dust tracers yield a *local* Σ_{SFR} lower by a factor of 50. The dust tracers yield much lower values (by a factor of ∼5) than both Hα due to the reduced dust abundance in the SMC.

The origin of the weak dust emission in NGC 346 is not the same as the weak emission in the Gould-belt SF regions reported by Vutisalchavakul & Evans (2013). These authors have compared the SFR one would derive from *Spitzer*/MIPS 24 μm measurements or TIR with SFR derived from counting YSOs. They find that the IR tracers underpredict the true SFR by two orders of magnitude, because these regions lack high-mass stars due to incomplete sampling of the IMF. NGC 346 is a very rich environment and does not have such a lack of high-mass stars.

The difference between young-star counts and the Hα derived values is due to the fact that the individual massive young stars in NGC 346 produce Hα (and dust) emission over a much larger surface than the size of the pixel in which they are counted, significantly larger than the full *HST* field of view. Note that this effect will cause the tight relation between SFR (derived from Hα) and the gas column density to break down on small (≲100 pc) scales, similar to what is observed in M33 (Onodera et al. 2010). This break-down occurs even in the absence of drifting of the stars from their birth environment or spread induced by evolutionary effects, simply because the local Hα (or dust) emission no longer measures the locally produced UV-radiation field. Fig. 6 demonstrates how large this distance is. We show the fraction of the SFR which is recovered when integrating the extinction-corrected Hα emission (based on the combination of Hα and 24 μm emission) in apertures of increasing radius. Within the *HST* field of view we recover 50 per cent. When we integrate out to a radius of 500 arcsec (145 pc), where the Hα emission from the NGC 346 complex becomes indistinguishable from the general SMC emission, we recover ∼90 per cent. In this calculation, we assume that outside the field of view of the *HST* observations, the SF is insignificant. This is corroborated by the results of Sewiło et al. (2013) who identified YSO candidates based on IR photometry of the entire SMC. Of the sources from their highly reliable YSO-candidate list which are associated with NGC 346, less than 20 per cent (4/23) are located outside of the field of view of *HST*. A very similar result is found when using the spectroscopically confirmed early-type stars from Bonanos et al. (2010). Of the 43 O-type stars from this catalogue within a 100 pc radius around NGC 346, only ∼15 per cent (6) are not within the field of view of *HST*.

We conclude that the total SFR as measured from the (predominantly low-mass) young-star counts is consistent with the SFR measured from Hα emission to within ∼10 per cent. However, the absorption of the hard radiation from the hot stars and subsequent re-emission as either recombination lines or dust continuum occurs far – at distances >100 pc, in the case of NGC 346 – from the actual location of these stars. See also Relaño et al. (2012) and Li et al. (2013) for excellent discussions on how radiation escaping the local environment affects Hα and dust emission as SFR tracers on small spatial scales. As a consequence, these indirect tracers which depend on absorption and re-emission cannot be used for our present purpose, which is to relate the stellar densities with the ISM on smaller scales within the star-forming complex. Note that most extragalactic studies that use Hα to derive SFR are probing much
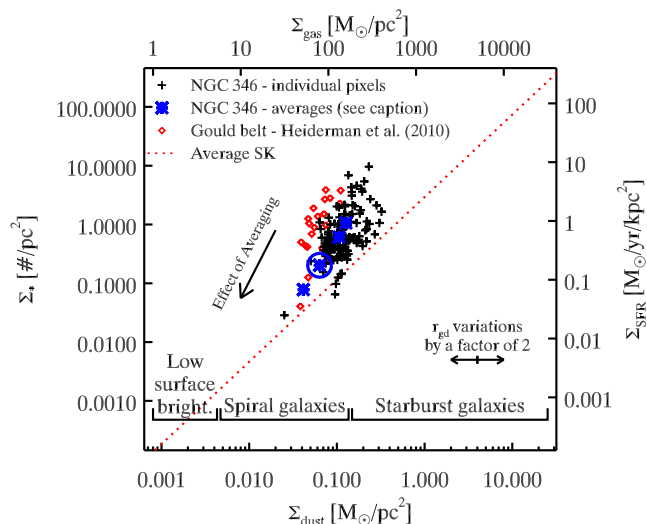

Figure 7. Scatter plot of surface density of young stars versus surface density of dust per pixel of 20×20 arcsec^2 (6×6 pc^2). The dotted line shows the 'standard' relation from Kennicutt & Evans (2012, fig. 11a). The values from Heiderman et al. (2010), based on YSO counts and ISM column densities in nearby individual molecular clumps, are also shown. The values for NGC 346 (black pluses) lie systematically above the 'standard' line. The thick blue stars indicate where NGC 346 is located when we average over all pixels in the masked area, and subsequently over apertures with radii of 52, 90 and 145 pc (from top right to bottom left). These radii correspond to the approximate size of the *HST* surveyed area, the prominent far-IR emission nebula and the size of the Hα nebula, respectively. The power-law exponent of the effect of averaging, i.e. the slope of the arrow in the figure, is 2.9.

larger regions (≳kpc) than the scale on which the indirect tracers are reconciled with the direct measurements (∼150 pc) and are thus unaffected by this effect.

5 COMPARISON OF GAS AND STARS

In the following section, we compare the derived SFR and ISM column densities. We first concentrate on the global behaviour and how NGC 346 compares to other measurements before looking in more detail at the tendencies within the complex.

5.1 Global comparison

We show in Fig. 7 the stellar surface density versus the dust surface density for each pixel. These are the basic observational quantities which do not depend on assumptions about M_{cat}, Δt_{SFR} or r_{gd}. Using the values in Table 1, we convert these into Σ_{SFR} and Σ_{gas} (right and top axes). The individual pixels within NGC 346 lie above the fiducial SK relation for Σ_{SFR} versus Σ_{HI+H_2} (Kennicutt & Evans 2012, fig. 11a) by on average a factor of 7. For reference, we also show the points for individual clumps in nearby Milky Way star-forming regions from Heiderman et al. (2010), which also lie consistently above the SK relation. These authors use SFR from low-mass YSOs and column densities from the dense gas measured from extinction maps on a typical scale of a few parsec. The fact that all these small-scale measurements lie above the galaxy-averaged values is expected (Kruijssen & Longmore 2014). The offset is due to the selection bias introduced by studying a region which is currently, actively forming stars, while the galaxy-averaged values include also regions which are not presently forming stars.

Compared to the study from Heiderman et al. (2010), our approach has the advantage of using the dust in *emission* to measure the column densities and that we have access to dust emission covering a large area surrounding the star-forming complex. This allows us to calculate averaged values over relevant spatial scales, taking into account also parts of the ISM which are less vigorously forming stars.

The thick blue stars correspond to averages over the entire masked area, the entire *HST* field of view, the prominent SPIRE 250 μm emission and the Hα nebula (top right to bottom left, respectively, see also Table 2). The mean value lies progressively closer to the SK relation as we increase the area over which we calculate the average. It should be noted that the same shifting to bottom left *must* occur also to the values from Heiderman et al. (2010) if they were to integrate to larger distance from their young stars (to lower column densities), as the conditions that prevail in their low-mass star-forming regions are probably more representative for the spiral galaxies at low Σ_{SFR} rather than those on the dividing line between the most active spirals and starburst galaxies. The third star from the top in Fig. 7 – highlighted by a circle – indicates the average over the area where significant cold dust emission is detected in excess to the general SMC emission. This is probably the best estimate of the average SFR and ISM column density for the complex in its entirety. This value is above the SK relation by about a factor of 3 albeit roughly compatible with the average relation when taking into account its scatter of 0.3 dex. This factor is consistent with the prediction from Kruijssen & Longmore (2014) for the size of the region ∼300 pc diameter over which we do the comparison. We also indicate in Fig. 7 by how much the NGC 346 values would be displaced (left-to-right) relative to the data from Heiderman et al. (2010) and the SK line as a result of a factor of 2 variations in r_{gd}. If r_{gd} were 2500 as opposed to 1250, the average values of NGC 346 would fall on the SK line. Such a high value for r_{gd} would imply that half of the total gas (more than 80 per cent of the molecular gas) within a 500 arcsec (145 pc) radius around NGC 346 is molecular without corresponding CO emission, as a result of photodissociation of the CO molecule. Such an large reservoir of hidden molecular gas, not related to CO, seems difficult to reconcile with the emission of C^+ which traces the photodissociation. Israel & Maloney (2011) show that the distribution of the [C II] 158 μm line emission closely resembles the CO distribution.

5.2 The physical origin of variations in stellar mass fraction

On the spatial scale that we probe here (∼6 × 6 pc²), we measure significant scatter in the relation between Σ_{gas} and $\Sigma_{M_\star}$ (Fig. 7). Such a scatter on small scales is expected, due to the stochastic nature of the local SF process, as well as relative motions between the formed stars and the reservoir from which they formed (Kruijssen & Longmore 2014). The observed scatter is more easily assessed in Fig. 8, where we concentrate on the values derived for NGC 346. This figure also shows the derived power law for the entire ensemble of sight-lines. We use the IDL routine MPFITEXY[7] (Williams, Bureau & Cappellari 2010) which uses MPFIT (Markwardt 2009) to determine a straight-line fit to the data (in log–log space) with uncertainties in both variables. The best-fitting value for the exponent is 2.6 ± 0.2, i.e. the relation is much steeper than the canonical SK relation (exponent ∼1.4). This very steep increase of Σ_{SFR} with Σ_{gas} is similar to the large exponents found by Gutermuth et al. (2011).
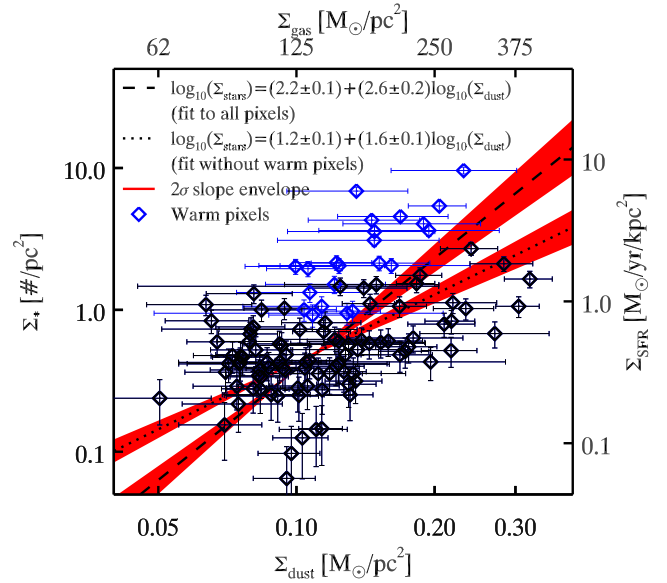
[7] http://purl.org/mike/mpfitexy

Figure 8. Scatter plot of surface density of young stars versus surface density of dust per pixel of 20 × 20 arcsec² (6 × 6 pc²) zoomed in on the range occupied by NGC 346. The blue points have a strong warm dust component in their SED ($\Sigma_{24\,\mu m}/\Sigma_{250\,\mu m}$ [F_ν/F_ν] > 0.3). Clearly, the lines of sight selected using this colour criterion occupy a separate region of the diagram. The long and short dashed lines are the straight-line fits in logarithmic space to the data with or without the warm pixels, respectively. The red areas correspond to the 2σ uncertainties of the best-fitting slope, while keeping the normalization fixed.
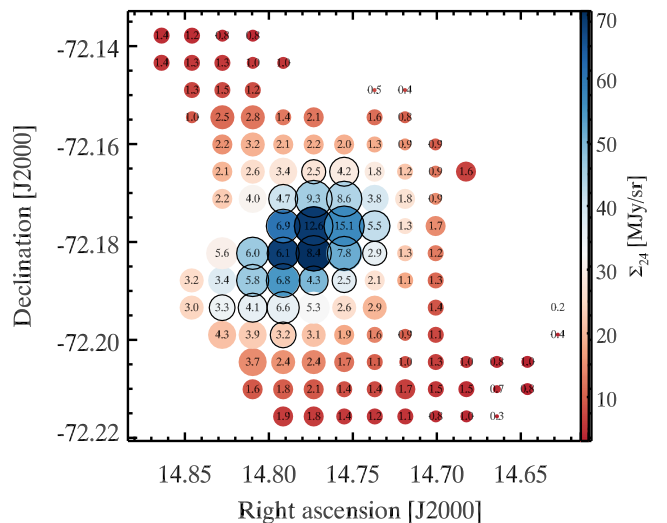

Figure 9. Map of the NGC 346 which shows the derived stellar mass fraction. The size of each point is dependent on frac$_{M_\star}$ and its colour depends on $\Sigma_{24\,\mu m}$. The mass fraction is indicated at each point. It is clear from this diagram that the stellar mass fraction peaks on the stellar cluster where the dust is heated to higher temperatures due to the intense radiation field. The warm pixels identified in Fig. 8 are encircled.

The observed variations in SFR at higher dust/gas surface densities are clearly correlated with other observables, in particular the dust colour temperature (here $\Sigma_{24\,\mu m}/\Sigma_{250\,\mu m}$ [Jy/Jy]). Perusal of the data shows that those pixels with $\Sigma_{24\,\mu m}/\Sigma_{250\,\mu m}$ >0.3, i.e. warm dust, are towards the rich stellar cluster and all exhibit high values in this diagram. The position of these warm sight-lines is also indicated in Fig. 9. We further show the power-law fit to the

data excluding the lines of sight with this very warm dust (exponent 1.6 ± 0.1). The derived exponent of the power law varies significantly depending on whether we include these sight-lines, which is an indication that the lines of sight towards the main cluster occupy a particular part of this diagram.

It is interesting to note that the rms scatter around the best-fitting power law is ± 0.4 dex. This is similar to the rms observed (± 0.3 dex) in the SK relation of integrated 'normal' spiral galaxies (Kennicutt & Evans 2012). Perhaps, some of the differences in physical conditions that underpin the variations among spiral galaxies are encountered within the NGC 346 star-forming complex. If this is indeed the case, then studies such as the one we present here offer a rare opportunity to zoom in to specific environments and determine the parameters that drive such variations.

In the following, we discuss the variations in terms of the stellar mass fraction of young stars ($\mathrm{frac}_{M\star} = \Sigma_{M\star} (\Sigma_{M\star} + \Sigma_{gas})^{-1}$) to facilitate comparison with star cluster formation models, where $\Sigma_{M\star}$ refers to the mass of the PMS+UMS stars. Moreover, we prefer this terminology over SFE, which concerns the time-averaged rate with which a large quantity of interstellar matter (entire complexes) is converted into stars. On the small scales we probe here, we measure the stars that have formed earlier and the remaining ISM column density. It is not evident that these stars have formed from the ISM we detect now along the line of sight nor that they will still be in this location, if and when the next generation of stars are born.

Across most of the surveyed area (66 per cent of the pixels) $\mathrm{frac}_{M\star}$ is below 2 per cent, with the most common value being 1 per cent,[8] see also Fig. 9. However, there is a significant tail to much higher values with a maximum of 15 per cent. These very high values correspond to very high stellar surface densities, *not* to low ISM column densities (see Fig. 4).

The observed variations in $\mathrm{frac}_{M\star}$ are certainly not random, but show a definite dependence on other measurable quantities. In particular, the highest values are found near the main cluster (Fig. 9). We also show the trend of stellar mass fraction as a function of distance to the main cluster in Fig. 10. Even though there are clear deviations from spherical symmetry in the region, we observe a monotonic decrease in $\mathrm{frac}_{M\star}$ with distance which can be approximated by a power law with exponent -0.7.

From the observations and the SED fitting, we have at our disposal a number of key probes that typify the conditions along the line of sight of each pixel. These range from quantities that measure directly the stellar densities and the resulting intense radiation field to those that depend on both the local radiation field and the ISM column density and state. In the same ordering, these probes are $\Sigma_\star$, $\Sigma_{24\,\mu m}$, the average radiation field ($\langle U \rangle$) as experienced by the dust grains,[9] Σ_{gas}, the molecular gas fraction and the molecular gas surface density. Perusal of the data shows that $\mathrm{frac}_{M\star}$ correlates well with stellar densities and hot dust emission at 24 μm (Figs 11a and b). The correlation with the ISM column density is much less tight (panel c), which is in part due to the fact that the amplitudes of variations in Σ_{gas} are much smaller than those in $\Sigma_\star$, i.e. the gas map is much flatter than the star map. When we use Σ_{CO}/Σ_{gas} as a proxy for the molecular gas fraction (panel d), there is no obvious correlation between the stellar mass fraction and the molecular
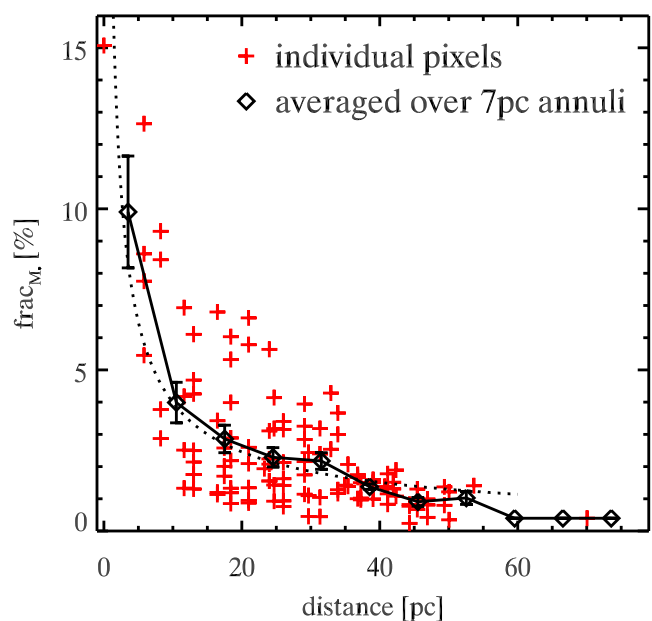

Figure 10. Trend of stellar mass fraction as a function of distance from the main cluster (RA = $14°755\ 179$, Dec. = $-72°171\ 201$ [J2000]). Individual pixel values are shown by red pluses. Annular-averaged values (in steps of 7 pc) are shown with black diamonds. The error bars shown are 1σ uncertainties on the mean. The behaviour can be approximated by $\mathrm{frac}_{M\star} = 0.2 \times \mathrm{distance}\ [\mathrm{pc}]^{(-0.7)}$ between ~ 1 and 55 pc (dashed line).

gas fraction. Specifically, the highest *and* the lowest stellar mass fractions coincide with intermediate values of the molecular gas fraction. The same is true also for the molecular surface density (panel e).

The basic conclusion we can draw is that the highest stellar mass fractions are found where the highest concentrations of stars are found, towards the central cluster. *There are many stars where there are many stars.* We find no obvious parameters of the current ISM towards the cluster that explain why the cluster formed there. It is neither the densest nor the most molecular ISM within the complex. Probably the strong radiation over the past few Myr has already erased the memory of the conditions that led to the formation of the cluster.

It should be noted that the central location of the main cluster may be a clue to why it formed there. It truly is central to the complex in most tracers. In the ISM column density tracers, in particular, the main cluster location appears as the intersecting 'hub' of three peripheral dense 'arms' (Figs 2 and 12). If the main cluster is indeed located at the meeting point of several dense arms, it possible that the SF process was/is being fed by these structures. Whether this is the case cannot be assessed without kinematic measurements of the dense gas.

6 POSSIBLE BIASES

We find that the stellar mass fraction is highest towards the rich central cluster. There are several effects and biases that could influence this interpretation.

6.1 Completeness

The derived relation between the newly formed stars and the ISM depends on the completeness of the *HST* stellar catalogue. The average completeness for stars which are too faint and crowding

---

[8] 1 per cent corresponds to a gas consumption time-scale of 5×10^8 yr, given the duration of the SF event of 5 Myr.

[9] $\langle U \rangle$ is the average field weighted by dust mass and as a result does not measure the ambient radiation field if the line-of-sight extinction is significant.
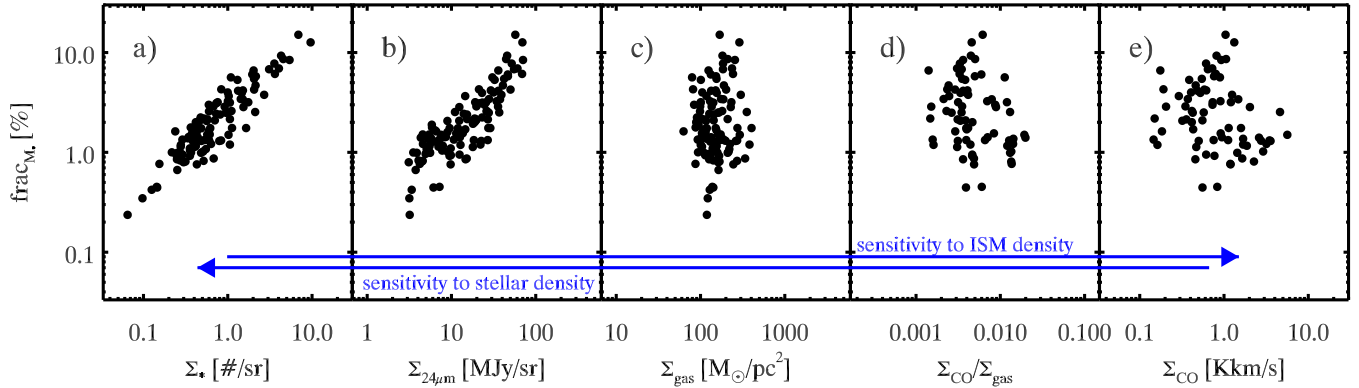
Figure 11. Scatter plots of the stellar mass fraction as a function of a number of key tracers. From left to right, the tracer measures increasingly the ISM density and the presence of dense clumps. From right to left, the sensitivity to the local stellar density increases. $\Sigma_\star$ is the surface density of the PMS+UMS stars. All panels span an identical dynamic range ($x_{max}/x_{min} = y_{max}/y_{min} = 1000$).
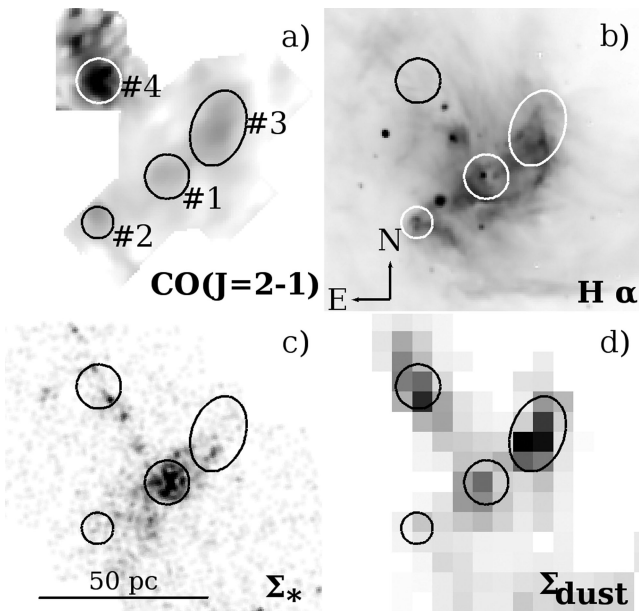

Figure 12. Distinct regions within the NGC 346 complex as observed in a number of key tracers: CO($J = 2$–1) integrated intensity map (Rubio et al. 2000, panel a), Hα emission (Smith et al. 2000, panel b), young-star density map based on Gouliermis et al. (2006, panel c) and the dust surface density (this work, panel d). All maps are shown in linear scale. We indicate four regions corresponding to local maxima in CO emission.

has been accounted for by integrating the completeness-corrected mass function (Sabbi et al. 2008, see also Section 3). If there are remaining incompleteness issues in the catalogue, the frac$_{M_\star}$ would be even higher than that we derive now. The observed variations in frac$_{M_\star}$ could be affected, if there are large spatial variations in completeness.

Crowding: The regions which could be affected by crowding more than the average are the regions of the highest stellar density. However, these regions already have the highest mass fraction of stars, and an additional correction would place these regions farther from the mean rather than closer.

Extinction: NGC 346 exhibits some sight-lines with significant amounts of dust (Fig. 12) which could hide embedded clusters of young stars. This could affect, in particular, the regions labelled #3 and #4. Both regions have a lower than average stellar mass fraction

and therefore additional embedded young stars would bring them closer to the average. However, the data argue against a significant population of embedded sources. First, because the peaks in the Σ_{dust} map do correspond to local peaks in the *HST* detected $\Sigma_\star$ map. Secondly, because there are no corresponding peaks in the MIPS 24 μm maps at these locations, while an embedded cluster would produce 24 μm emission. This emission would be detectable unimpeded by line-of-sight extinction. Finally, these regions have low observed dust temperatures, while embedded heating sources would increase their temperature.

6.2 Variations in gas-to-dust mass ratio

If there are significant and systematic variations in r_{gd}, the conversion from Σ_{dust} to Σ_{gas} would be affected. Specifically, if the dust in the central part has been mostly destroyed, we would grossly underestimate the Σ_{gas} there, which would bring these points closer to the general trend (to the right in Fig. 8). The SED modelling shows that these regions are extremely depleted in PAHs. Is it plausible that the dust has also been destroyed? The increase required in the assumed value of r_{gd} for the central region of NGC 346 in order to make the variations in frac$_{M_\star}$ disappear is a factor of 10 (r_{gd} equal to 12 500 instead of 1250).

An argument against significant dust destruction (or more generally significant variations in r_{gd}) is the very similar behaviour of Hα and TIR (and 24 μm) emission. The rms of $\Sigma_{TIR}/\Sigma_{H\alpha}$ of the 115 pixels across the whole region is only 20 per cent, and its behaviour is not spatially correlated with the stellar density or the radiation field density. This similar behaviour is also reflected in Fig. 5.[10] For the relatively low extinction conditions in NGC 346, $\Sigma_{H\alpha}$ measures the chance for the starlight to be absorbed locally by the gas and Σ_{TIR} measures the same for the dust; the very similar behaviour (on scales of 6×6 pc^2) of these tracers suggests a similar proportion of dust to gas across the region we studied. In case of very reduced dust abundances towards the central region, one would expect a limb-brightened shell in the dust emission, contrary to what is observed (Fig. 4a).

---

[10] The scatter in $\Sigma_{TIR}/\Sigma_{H\alpha}$ of 20 per cent is much smaller than the scatter – about the mean trend in Fig. 5 – in the Σ_{TIR} and $\Sigma_{H\alpha}$, individually. This indicates that an above (below) average value of $\Sigma_{H\alpha}$ corresponds to an above (below) average value in Σ_{TIR}.

A relatively constant r_{gd} is further supported by the analysis of Lebouteiller et al. (2008) who measured the gas phase abundances along 13 different sight-lines across the NGC 346 complex. They find only minor variations in the gas phase abundances. Most importantly they find only 0.1 dex variations in the S/H ratio while sulphur can be depleted into dust grains and strongly varying dust abundances would lead to variations of the abundance of sulphur remaining in the gas phase. We conclude that variations in r_{gd} that could explain the variations in $frac_{M\star}$ are improbable.

7 DISCUSSION

7.1 Effects of evolution

Our observations provide a snapshot of NGC 346 at one instance, roughly 3–5 Myr after the onset of the main SF event. During the SF epoch, the amount of gas transformed into stars *must* evolve. Is the observed scatter in $frac_{M\star}$ caused by studying only this snapshot? In other words, is it possible that after the SF has ceased, the $frac_{M\star}$ will be more homogeneous? Within the complex, different regimes can be discerned, as is illustrated in Fig. 12.

(i) *Region #1:* Main cluster with high dust surface densities and high number of stars. The region is detected in CO with moderate brightness.

(ii) *Region #2:* Secondary cluster with fewer stars and less dust. Appears to be a 'scaled-down' version of the main cluster with bright Hα and MIPS 24 μm emission and a moderately high $frac_{M\star}$.

(iii) *Region #3:* This blob to the north-west of the complex has the highest dust surface density and low measured $frac_{M\star}$. It is detected in CO but the estimated molecular gas fraction is low.

(iv) *Region #4:* The molecular 'spur' to the north-east has a small stellar mass fraction, high dust surface and no associated Hα emission.

It is unlikely that these regions will all produce the same stellar mass fraction in the end. It can be argued that region #4, with its low current $frac_{M\star}$ but large reservoir of molecular gas, has the potential to still form a significant number of stars and thus boost its final mass fraction. However, the conditions in regions #1–#3 do not seem to favour prominent continued SF. Their ISM seems lacerated with ionized gas, as testified by the prominent Hα emission and based on the CO map the molecular gas fraction is also low. We assess that, most likely, the observed differences between regions #1 and #3 will persist.

7.2 Gas removal and stellar motions

We find a clear trend in stellar mass fraction from the central parts of NGC 346 to its outskirts. Within ∼15 pc $frac_{M\star} \approx 10$ per cent while between 15 and 50 pc it is ∼2 per cent. These zones are dominated by the cluster and the dispersed young stellar population, respectively, as shown with the autocorrelation analysis of the stellar distribution (Gouliermis et al. 2014). The observed decrease of $frac_{M\star}$ with distance from the cluster is a signpost of lower SFE on the periphery (dispersed SF) than in the densest central parts (clustered SF). However, there are two caveats to consider, both related to the relative displacement of the stars and the ISM after birth.

A naive explanation for the present-day systematic behaviour of the stellar mass fraction is the accumulation of stars, born in the periphery, in the central cluster. If such a process was possible, it would boost the observed $frac_{M\star}$ in the cluster while reducing its

value outside. However, this is an implausible scenario. Consider the free-fall time (τ_{ff}) of a star born in the periphery to be pulled into the cluster by gravity:

$$\tau_{ff} = \frac{\pi}{2} \frac{d^{3/2}}{\sqrt{GM_{cl}}}, \tag{2}$$

where d is the distance from the cluster, M_{cl} is the mass of the cluster (gas plus stars) and G is the gravitational constant. τ_{ff} is the *shortest* time-scale for a star to migrate towards the cluster, ignoring friction, virial velocities, rotational motions and the existence of any matter outside of the cluster that will exercise gravitational pull. For the observed M_{cl} of ∼10^5 M$_\odot$ (= $N_{\star<15 pc} M_{cat} frac_{M\star}^{-1}$ = 2300 × 4.3/0.1) and a distance of 30 pc (the distance between regions #1 and #3 in Fig. 12), $\tau_{ff} \approx 9$ Myr, considerably longer than the ages of the PMS stars.

The second effect that could alter the observed $frac_{M\star}$ over time is gas removal from the central region. When a cluster is formed, the gas left over from the SF process may be rapidly removed by stellar winds (Lada, Margulis & Dearborn 1984). More recent work, however, suggests that the winds (and later, supernovae) may escape through low-density channels formed in a hierarchical ISM (e.g. Rogers & Pittard 2013; Dale et al. 2014) causing much of the residual gas to remain. This seems to be the case for NGC 346. *HST* images of NGC 346 in the light of Hα show the presence of residual gas. Molecular gas also appears to be present in the centre of the cluster despite the proximity of O stars (Fig. 12). *Chandra* observations reveal a low diffuse X-ray flux (Nazé et al. 2002), which indicates that either that a supernova explosion has yet to occur or the hot gas has escaped the region. Therefore, gas expulsion cannot have produced the position dependence of $frac_{M\star}$. In further support of this conclusion are the findings of Smith (2012) and Smith et al. (in preparation). These authors present high spectral resolution observations of Hα and [O III] to examine the ionized gas motions in NGC 346. They find that the gas is quiescent. Data over 10 slit positions covering the ionized nebula show no evidence for velocity splitting, even at the centre of the cluster. These results indicate that the gas is not being expelled by stellar winds but rather the dominant form of interaction is via stellar radiation to produce a classical expanding H II region.

An additional argument against the importance of efficient gas removal leading to a cavity in the central part of our map comes from the *Spitzer* detected embedded YSO candidates (Simon et al. 2007; Sewiło et al. 2013). These sources are young (≲1 Myr) and several of them are detected towards the central cluster. The number of detected YSO candidates towards the centre of NGC 346 is probably a lower limit, set by the difficulty of detecting individual point sources which exhibit a mid-IR excess in the crowded cluster region against the strong extended emission component due to the hot dust. The SFR derived from these objects (>3.2×10^{-3} M$_\odot$ yr^{-1}; Simon et al. 2007) is fully compatible with the average SFR for the entire 5 Myr event. If the clearing of the natal gas had taken place, one would expect to find few of these very young sources towards the central part of our map and probably also a diminishing trend of the SFR.

We conclude that the difference of a factor of ∼5 in observed $frac_{M\star}$ most likely reflects a real difference in the average SFE in the clustered versus the dispersed star-forming regimes. This finding is consistent with theoretical models that assume that the SFE is proportional to the free-fall time; hence, denser regions have higher efficiencies (e.g. Elmegreen 2000; Krumholz & Tan 2007; Kruijssen 2012; Federrath 2013; Hopkins 2013).

7.3 High SFE – linked to low metallicity?

The SFE of NGC 346 is high even after averaging over ~150 pc (radius) scales (Fig. 7). As discussed in Kruijssen & Longmore (2014), this may be explained by the bias introduced by having chosen an active star-forming complex as the object of study. These authors predict an offset of a factor of ~3 for the size of the regions we study, similar to what is observed. Additionally, this high value may be related to an above average SFE in the clustered environment which dominates NGC 346. Nevertheless, it is still interesting to discuss the possible role of the lower metallicity for the following reasons. (i) Kennicutt (2008) shows that low-metallicity galaxies like the SMC, as a whole, lie a bit (factor of ~3) above the general SK relation. (ii) The largest radius we measured is 150 pc. It is not obvious that by averaging to a larger distance, the derived SFE will decrease significantly – as it is also not obvious that it will stay high – because the next prominent star-forming complex (LHA 120-N76) is only about 300 pc projected distance away from NGC 346.

Because the SFE within individual star-forming clouds is a critical parameter for theories of galaxy evolution and galactic-scale SF, with observable consequences on for example the galaxy luminosity function, there are many recent studies that have tried to assess whether the conversion of gas to stars depends on local ISM conditions and/or global galaxy parameters. Saintonge et al. (2011) investigated the global gas content and SFRs in ~200 galaxies in the redshift range between 0.025 and 0.05, finding a clear decrease in the SFE with increasing stellar mass. Resolved studies of nearby galaxies, meanwhile, have shown that the SFE on ~kpc scales varies with several ISM and Galactic-scale parameters, including stellar mass, dust-to-gas ratio, rotation velocity, orbital time and Hubble type (e.g. Leroy et al. 2013).

While the influence of any one parameter is difficult to isolate, a general conclusion that can be drawn from these studies is that low-mass, low-metallicity, late-type galaxies appear to be more efficient at forming stars from their molecular reservoir than high-mass, metal-rich, early-type disc galaxies. This could be in part a direct effect of metallicity: Dib (2011) shows that low-metallicity star-forming regions may lie above the SK relation for normal metallicity galaxies by a factor of 0.3 dex as a consequence of higher SFE caused by less effective removal of the gas from the star-forming region by stellar winds at low metallicity (Dib et al. 2011). The observed trend may also be due to an increasing fraction of molecular material located outside bound star-forming structures as the stellar mass and hence ISM pressure increases, although other effects are likely to contribute to the observed trends.

Our results in Section 5.1 are consistent with the picture emerging from lower resolution studies that molecular gas in low-metallicity, low-mass systems is somewhat more efficient at forming stars. In our case, we find that the mass of young stars in NGC 346 is high relative to its gas content, even after we average our measurements over scales that approach the spatial resolution of nearby galaxy surveys. However, we caution the reader to realize that the presented analysis of NGC 346 alone does not allow us to derive the global SMC SFE nor conclude that it is above average.

8 SUMMARY

We present a detailed comparison of the surface density of young (PMS+UMS) stars ($\Sigma_\star$) and dust surface density (Σ_{dust}) across the face of the most prominent star-forming complex NGC 346 (N66) in the SMC. $\Sigma_\star$ is derived from individual stars identified in the CMD based on *HST* photometry. Σ_{dust} is obtained via radiative transfer modelling of the IR-to-submm SED. We measure these quantities in 115 independent pixels of 6×6 pc^2 out to distances of ~50 pc from the main cluster, covering an area of >4000 pc^2.

We find a correlation between $\Sigma_\star$ as a function of Σ_{dust} with a considerable scatter. A power-law fit to the data yields a steep relation with an exponent of 2.6 ± 0.2. We find that sight-lines towards the central $\lesssim 15$ pc exhibit *systematically* high values of $\Sigma_\star / \Sigma_{dust}$ by a factor of ~5 compared to the rest of the complex.

We convert $\Sigma_\star$ to average star formation rate (SFR) surface densities (Σ_{SFR} in M$_\odot$ yr^{-1} pc^{-2}) using (1) the observed mass function to derive the total stellar mass formed and (2) the time span over which these young stars have formed (5 Myr). This Σ_{SFR} is much less biased to the contribution of high-mass stars than luminosity-based SFR tracers. The derived total SFR ($4 \pm 1 \times 10^{-3}$ M$_\odot$ yr^{-1}) is consistent (within 10 per cent) with Σ_{SFR} estimated from the extinction-corrected Hα emission integrated over the entire Hα nebula.

On small scales (6×6 pc^2) the SFR estimated from indirect tracers (ionized gas or dust emission) compares very poorly with the SFR based on star counts. Across most of the studied region, Hα systematically underestimates the local SFR, reaching a factor of 10 discrepancy in the central part of the complex. This discrepancy is due to ionizing photons escaping the local volume where the young stars are counted.

We convert Σ_{dust} to gas surface density (Σ_{gas}) using a constant gas-to-dust mass ratio ($r_{gd} = 1250$). This value is calibrated on our dust SED fitting method to yield the measured gas mass (from H$\,$I and CO) on a large scale, within a 500 arcsec radius centred on NGC 346. On this scale most of the gas mass is contained in the atomic phase and the influence of the uncertain conversion factor from CO intensity to H$_2$ column density is small.

Using the derived Σ_{gas} and Σ_{SFR}, we place the pixels on an SK diagram. We find that individual pixels fall systematically above the SK relation for integrated disc galaxies by on average a factor of ~7. This offset decreases as larger beams are used, consistent with the prediction from Kruijssen & Longmore (2014).

The observed offset is reminiscent of the results of Heiderman et al. (2010) and Wu et al. (2010) who show that the measured SFR lies above the galaxy averages when 'zooming-in' to parsec scale on star-forming clumps in the Milky Way. This is probably caused by less dense gas, which is inefficient in forming stars, that is included in the galaxy-scale averages but not included when 'zooming-in' on individual clumps. A main difference with our analysis is that, even though we analyse 6×6 pc^2 sized regions, we cover the full star-forming complex and find that the entire active region (~50 pc) lies consistently above the relation. In other words, for NGC 346 one needs to 'zoom-out' beyond 50 pc to probe this less dense, non-star-forming gas. The average over a larger area (90 pc radius) lies closer to the SK relation but remains high by a factor of ~3.

We present a map of the observed stellar mass fraction (frac$_{M_\star}$ = $\Sigma_\star$ (Σ_{gas} + $\Sigma_\star$)$^{-1}$). frac$_{M_\star}$ is systematically high (~10 per cent) within the central 15 pc of the complex and systematically lower outside (2 per cent). We interpret this difference as the results of a higher SFE in the central zone. The inner 15 pc is dominated by young stars belonging to a centrally condensed cluster, while the outer parts are dominated by a dispersed population (Gouliermis et al. 2014). Therefore, the observed behaviour could reflect a change in SFE between clustered and non-clustered SF.

ACKNOWLEDGEMENTS

REFERENCES

Bernard J.-P. et al., 2008, AJ, 136, 919
Bolatto A. D., Wolfire M., Leroy A. K., 2013, ARA&A, 51, 207
Bonanos A. Z. et al., 2010, AJ, 140, 416
Calzetti D. et al., 2007, ApJ, 666, 870
Chen C.-H. R. et al., 2010, ApJ, 721, 1206
Chen C.-H. R. et al., 2014, ApJ, 785, 162
Cignoni M., Tosi M., Sabbi E., Nota A., Gallagher J. S., 2011, AJ, 141, 31
Clark P. C., Glover S. C. O., 2014, MNRAS, 444, 2396
Dale D. A., Helou G., Contursi A., Silbermann N. A., Kolhatkar S., 2001, ApJ, 549, 215
Dale J. E., Ngoumou J., Ercolano B., Bonnell I. A., 2014, MNRAS, 442, 694
Dib S., 2011, ApJ, 737, L20
Dib S., Piau L., Mohanty S., Braine J., 2011, MNRAS, 415, 3439
Dickel J. R., Gruendl R. A., McIntyre V. J., Amy S. W., 2010, AJ, 140, 1511
Draine B. T., Li A., 2007, ApJ, 657, 810
Elmegreen B. G., 2000, ApJ, 530, 277
Evans N. J., II, et al ., 2009, ApJS, 181, 321
Federrath C., 2013, MNRAS, 436, 3167
Galametz M. et al., 2013, MNRAS, 431, 1596
Galliano F. et al., 2011, A&A, 536, A88
Goodman A. A., 2004, in Johnstone D., Adams F. C., Lin D. N. C., Neufeeld D. A., Ostriker E. C., eds, ASP Conf. Ser. Vol. 323, Star Formation in the Interstellar Medium: In Honor of David Hollenbach. Astron. Soc. Pac., San Francisco, p. 171
Gordon K. D. et al., 2011, AJ, 142, 102
Gordon K. D. et al., 2014, ApJ, 797, 85
Gouliermis D. A., 2012, Space Sci. Rev., 169, 1
Gouliermis D. A., Dolphin A. E., Brandner W., Henning T., 2006, ApJS, 166, 549
Gouliermis D. A., Hony S., Klessen R. S., 2014, MNRAS, 439, 3775
Gutermuth R. A., Pipher J. L., Megeath S. T., Myers P. C., Allen L. E., Allen T. S., 2011, ApJ, 739, 84
Hao C.-N., Kennicutt R. C., Johnson B. D., Calzetti D., Dale D. A., Moustakas J., 2011, ApJ, 741, 124
Harries T. J., Hilditch R. W., Howarth I. D., 2003, MNRAS, 339, 157
Haser S. M., Pauldrach A. W. A., Lennon D. J., Kudritzki R.-P., Lennon M., Puls J., Voels S. A., 1998, A&A, 330, 285
Heiderman A., Evans N. J., II, Allen L. E., Huard T., Heyer M., 2010, ApJ, 723, 1019
Hony S. et al., 2010, A&A, 518, L76
Hopkins P. F., 2013, MNRAS, 428, 1950
Indebetouw R. et al., 2008, AJ, 136, 1442
Israel F. P., Maloney P. R., 2011, A&A, 531, A19
Jeffries R. D., 2012, in Moitinho A., Alves J., eds, Are There Age Spreads in Star Forming Regions? Springer-Verlag, Berlin, p. 163
Kennicutt R. C., Jr 2008, in Knapen J. H., Mahoney T. J., Vazdekis A., eds, ASP Conf. Ser. Vol. 390, Pathways Through an Eclectic Universe. Astron. Soc. Pac., San Francisco, p. 149
Kennicutt R. C., Evans N. J., 2012, ARA&A, 50, 531
Kim S., Staveley-Smith L., Dopita M. A., Sault R. J., Freeman K. C., Lee Y., Chu Y.-H., 2003, ApJS, 148, 473
Kiseleva L. G., Colin I., Dauphole B., Eggleton P., 1998, MNRAS, 301, 759
Kroupa P., 2001, MNRAS, 322, 231
Kruijssen J. M. D., 2012, MNRAS, 426, 3008
Kruijssen J. M. D., Longmore S. N., 2014, MNRAS, 439, 3239
Krumholz M. R., Tan J. C., 2007, ApJ, 654, 304
Lada C. J., Margulis M., Dearborn D., 1984, ApJ, 285, 141
Lada C. J., Lombardi M., Alves J. F., 2010, ApJ, 724, 687
Lebouteiller V., Bernard-Salas J., Brandl B., Whelan D. G., Wu Y., Charmandaris V., Devost D., Houck J. R., 2008, ApJ, 680, 398
Leroy A. K. et al., 2013, AJ, 146, 19
Li Y. et al., 2013, ApJ, 768, 180
Longmore S. N. et al., 2013, MNRAS, 429, 987
Markwardt C. B., 2009, in Bohlender D. A., Durand D., Dowler P., eds, ASP Conf. Ser. Vol. 411, Astronomical Data Analysis Software and Systems XVIII. Astron. Soc. Pac., San Francisco, p. 251
Massey P., Parker J. W., Garmany C. D., 1989, AJ, 98, 1305
Mathis J. S., Mezger P. G., Panagia N., 1983, A&A, 128, 212
Mauch T., Murphy T., Buttery H. J., Curran J., Hunstead R. W., Piestrzynski B., Robertson J. G., Sadler E. M., 2003, MNRAS, 342, 1117
Meixner M. et al., 2013, AJ, 146, 62
Mokiem M. R. et al., 2006, A&A, 456, 1131
Murphy E. J. et al., 2011, ApJ, 737, 67
Nazé Y., Hartwell J. M., Stevens I. R., Corcoran M. F., Chu Y.-H., Koenigsberger G., Moffat A. F. J., Niemela V. S., 2002, ApJ, 580, 225
Nota A. et al., 2006, ApJ, 640, L29
Onodera S. et al., 2010, ApJ, 722, L127
Planck Collaboration XVII, 2011, A&A, 536, A17
Preibisch T., 2012, Res. Astron. Astrophys., 12, 1
Rathborne J. M. et al., 2014, ApJ, 786, 140
Reid W. A., Payne J. L., Filipović M. D., Danforth C. W., Jones P. A., White G. L., Staveley-Smith L., 2006, MNRAS, 367, 1379
Relaño M., Kennicutt R. C., Jr, Eldridge J. J., Lee J. C., Verley S., 2012, MNRAS, 423, 2933
Rieke G. H., Alonso-Herrero A., Weiner B. J., Pérez-González P. G., Blaylock M., Donley J. L., Marcillac D., 2009, ApJ, 692, 556
Rogers H., Pittard J. M., 2013, MNRAS, 431, 1337
Rubio M., Contursi A., Lequeux J., Probst R., Barbá R., Boulanger F., Cesarsky D., Maoli R., 2000, A&A, 359, 1139

Sabbi E. et al., 2008, AJ, 135, 173

Saintonge A. et al., 2011, MNRAS, 415, 61

Sandstrom K. M., Bolatto A. D., Draine B. T., Bot C., Stanimirović S., 2010, ApJ, 715, 701

Sauvage M., Vigroux L., Thuan T. X., 1990, A&A, 237, 296

Scalo J. M., 1986, Fund. Cosmic Phys., 11, 1

Schuller F., Nord M., Vlahakis C., Albrecht M., Beelen A., Bertoldi F., Müller S., Schaaf R., 2010, BoA – The Bolometer Data Analysis Software: User and Reference Manual, 4th edn. ESO, Garching, Germany

Sewiło M. et al., 2013, ApJ, 778, 15

Simon J. D. et al., 2007, ApJ, 669, 327

Smith L. J., 2012, in Drissen L., Rubert C., St-Louis N., Moffat A. F. J., eds, ASP Conf. Ser. Vol. 465, Proceedings of a Scientific Meeting in Honor of Anthony F. J. Moffat. Astron. Soc. Pac., San Francisco, p. 416

Smith C., Leiton R., Pizarro S., 2000, in Alloin D., Olsen K., Galaz G., eds, ASP Conf. Ser. Vol. 221, Stars, Gas and Dust in Galaxies: Exploring the Links. Astron. Soc. Pac., San Francisco, p. 83

Vutisalchavakul N., Evans N. J., II, 2013, ApJ, 765, 129

Williams M. J., Bureau M., Cappellari M., 2010, MNRAS, 409, 1330

Wu J., Evans N. J., II, Shirley Y. L., Knez C., 2010, ApJS, 188, 313

Zubko V. G., Mennella V., Colangeli L., Bussoletti E., 1996, MNRAS, 282, 1321

Zubko V., Dwek E., Arendt R. G., 2004, ApJS, 152, 211

[1] *Institut für Theoretische Astrophysik, Zentrum für Astronomie, Universität Heidelberg, Albert-Ueberle-Str. 2, D-69120 Heidelberg, Germany*

[2] *Max Planck Institute for Astronomy, Königstuhl 17, D-69117 Heidelberg, Germany*

[3] *Laboratoire AIM, CEA/IRFU/Service d'Astrophysique, Université Paris Diderot, Bat. 709, 91191 Gif-sur-Yvette, France*

[4] *European Southern Observatory, Karl-Schwarzschild-Str. 2, D-85748 Garching-bei-München, Germany*

[5] *Max-Planck-Institut für Radioastronomie, Auf dem Hügel 69, D-53121 Bonn, Germany*

[6] *Niels Bohr International Academy, Niels Bohr Institute, Blegdamsvej 17, DK-2100 Copenhagen, Denmark*

[7] *Centre for Star and Planet Formation, University of Copenhagen, Øster Voldgade 5-7, DK-1350 Copenhagen, Denmark*

[8] *CNRS, IRAP, 9 Av. Colonel Roche, BP 44346, 31028 Toulouse Cedex 4, France*

[9] *Université de Toulouse, UPS-OMP, IRAP, 31028 Toulouse Cedex 4, France*

[10] *Department of Astronomy and Astrophysics, University of California, 1156 High Street, Santa Cruz, CA 95064, USA*

[11] *Kavli Institute for Particle Astrophysics and Cosmology, Stanford University, SLAC National Accelerator Laboratory, Menlo Park, CA 94025, USA*

[12] *Space Telescope Science Institute, 3700 San Martin Drive, Baltimore, MD 21218, USA*

[13] *Space Telescope Science Institute and European Space Agency, 3700 San Martin Drive, Baltimore, MD 21218, USA*

[14] *Observatoire astronomique de Strasbourg, Université de Strasbourg, CNRS, UMR 7550, 11 rue de l'Université, 67000 Strasbourg, France*

[15] *Department of Astronomy, University of Virginia, PO Box 3818, Charlottesville, VA 22903, USA*

[16] *Sterrenkundig Observatorium, Universiteit Gent, B-9000 Gent, Belgium*

[17] *National Radio Astronomical Observatory, Charlottesville, VA 22904, USA*

[18] *Department of Physics and Astronomy, The Johns Hopkins University, 366 Bloomberg Center, 3400 N. Charles Street, Baltimore, MD 21218, USA*

[19] *School of Physical & Geographical Sciences, Lennard-Jones Laboratories, Keele University, Staffordshire ST5 5BG, UK*

[20] *Departamento de Astronomia, Universidad de Chile, Casilla 36-D, Santiago, Chile*

[21] *Department of Astronomy, Graduate School of Science, The University of Tokyo, Bunkyo-ku, Tokyo 113-0033, Japan*

This paper has been typeset from a TEX/LATEX file prepared by the author.